Electron density distribution and static dipole moment of $KNbO_3$ at high pressure

T. Yamanaka,[1,2,3,*] T. Okada,[2] and Y. Nakamoto[3]
[1]*Geophysical Laboratory, Carnegie Institution of Washington, Washington DC, 20015-1305 USA*
[2]*Department of Earth and Space Science, Osaka University, Osaka, 560-0043 Japan*
[3]*Center for Quantum Science and Technology Under Extreme Conditions, Osaka University, Osaka, 560-0043 Japan*
(Received 25 October 2008; published 24 September 2009)

The electron-density distribution of single-crystal $KNbO_3$ has been measured as a function of pressure using synchrotron-radiation techniques in order to understand the variation in its static dielectric properties. $KNbO_3$ adopts three different polymorphs at varying pressures and ambient temperature: the ambient pressure phase adopts an orthorhombic *Cm*2*m* (*Amm*2) structure that transforms to a tetragonal (*P*4*mm*) phase at about 7.0 GPa, which then transforms further to a cubic *Pm*3*m* phase at about 10.0 GPa. The cubic phase is paraelectric, while the two lower-pressure phases are ferroelectric. Difference Fourier and maximum entropy method maps clearly show *d*-*p*-π hybridization, which is composed of Nb 4*d* and O 2*p* states. The ferroelectric-to-paraelectric transition in $KNbO_3$ at high pressure is discussed with reference to the variation in the electron-density distribution with pressure. Covalent bonding is reduced in the tetragonal phase as valence electrons become more localized with increasing pressure. The effective charge calculated from the valence electron density indicates that the tetragonal phase has the largest dipole moment among the three polymorphs. Orientation of the polarization in the tetragonal phase is possible in the [001] direction as a result of strain, but the orthorhombic phase shows a considerably strong polarization in both the [010] and [001] directions. In the cubic phase, a statistical distribution of Nb atoms around the inversion center in the [001] and [110] directions, rather than the [111] direction, results in paraelectric character.

DOI: 10.1103/PhysRevB.80.094108 PACS number(s): 61.50.Ks, 63.70.+h, 77.84.−s, 77.80.Dj

I. INTRODUCTION

Numerous studies of phase transitions in classic ferroelectrics such as $BaTiO_3$, $PbTiO_3$, and $KNbO_3$ have been performed as functions of temperature and pressure using a number of different methods. Mechanisms of sequential phase transitions in ABO_3 perovskites have been rationalized by invoking the soft-mode[1] behavior and order-disorder on the *B* atom site,[2] with structural changes induced by electron-phonon interactions. $KNbO_3$ exhibits three structural transitions with decreasing temperature at ambient pressure: the cubic (*Pm*3*m*) phase transforms to a tetragonal (*P*4*mm*) phase at 691 K, which then adopts an orthorhombic (*Cm*2*m*) structure at 498 K. A final transition to a rhombohedral (*R*3*m*) structure takes place at 263 K.[3] The cubic phase is paraelectric, while the other three phases are all ferroelectric. Transitions between these phases with decreasing temperature are induced by either very small atomic displacements or small distortions of polyhedra that reduce the overall crystallographic symmetry. The $KNbO_3$ polymorphs are isostructural with corresponding phases of $BaTiO_3$ and undergo the same sequence of phase transitions with changing temperature.[4,5]

A crystal-structure investigation carried out under static compression remains the primary experimental method for determining the dynamical and elastic properties of a ferroelectric material, and a large amount of work has been devoted to understanding the pressure-induced structural transformations of ferroelectric materials in the $PbTiO_3$ system.[6–11] High pressure and low-temperature x-ray and neutron-powder-diffraction studies of the phase diagrams and equations of state for $KNbO_3$ polymorphs employing diamond-anvil cell (DAC) techniques have also been reported.[12–18]

Raman spectroscopy has also been widely used to elucidate soft phonon modes and relaxation modes of displacive and order-disorder transitions in ferroelectric materials, and a number of Raman studies of $KNbO_3$ have been carried out at high pressure.[12,19–22] X-ray-absorption fine-structure (XAFS) analysis has also been used to document local structural changes at high pressures and temperatures. Dielectric constant measurements have also been performed.[23–27] Numerous contributions toward understanding ferroelectric properties have been provided by novel theories, as well as first-principles electronic structure calculations.[28–30] *Ab initio* computations at varying pressures and temperatures have been targeted toward understanding the effects of short- and long-range orderings, the structural distortions, the nature of chemical bonding, and the role of phonon-lattice interactions in structural transitions.

Meanwhile, synchrotron-radiation (SR) facilities have accelerated the development of high-pressure crystallography as a result of their great advantages for diffraction studies under nonambient conditions. We report here the results of precise single-crystal x-ray diffraction experiments whose goal was to determine the electron-density distribution by the maximum entropy method (MEM) using single-crystal diffraction intensities. The space- and time-averaged structures of the dynamical vibration of the constituent atoms can be elucidated by x-ray diffraction from the electron-density distribution. The magnitude of the static dipole moment of the bulk crystal is then related to the change in the interatomic distances and effective charges.

II. EXPERIMENTAL

A. Single-crystal diffraction using synchrotron radiation

To understand the static polarization of a ferroelectric material, precise diffraction-intensity measurements are essential for determining a reliable electron-density distribution

TABLE I. Experimental conditions and result of the structure refinement (lattice parameters, atomic positional coordinates, and temperature factors). The reliability factors R (%) and wR (%) of the least-squares refinement presented in the end table are $R=\Sigma|(|F_{obs}|-|F_{cal}|)/\Sigma|F_{obs}|$ and $wR=\Sigma w(|F_{obs}|-|F_{cal}|)/\Sigma w|F_{obs}|$, where $w=1/\sigma^2|(F_{obs})|$, σ is a standard deviation of the observed intensity.

Pressure (GPa)	0.0001	1.6	4.8	5.7	7.6	9.4	10.9
Structure type		Orthorhombic			Tetragonal		Cubic
Space group	*Cm*2*m*	*Cm*2*m*	*Cm*2*m*	*Cm*2*m*	*P*4*mm*	*P*4*mm*	*Pm*3*m*
Dielectricity	Ferro	Ferro	Ferro	Ferro	Ferro	Ferro	Para
Diffractometer	AFC6S	AFC5R	AFC5R	AFC5R	AFC5R	PF-BL10A	PF-BL10A
Wavelength (Å)	0.71069	0.71069	0.71069	0.71069	0.71069	0.61907	0.61907
Receiving slit	1°	1°	1°	1°	5 mmϕ	1.5 mmϕ	1.5 mmϕ
2θ range (deg)	120	85.6	87.2	80.1	80.4	86.2	82.8
	bisec	ϕ fixed	ϕ fixed	ϕ fixed	ϕ fixed	ϕ fixed	f fixed
Scan width			1.37+0.3 tan θ		1.6	1.2	1.2
Scan speed	2°/min	1°/min	1°/min	1°/min	1°/min	0.01°/s	0.01°/s
Gasket		Spring steel	Spring steel	Re	Re	Re	Re
Pressure media			Metha-etha				
Culet size		500	500	400	400	400	400
Crystal size (μm^3)	$120\times100\times80$	$130\times90\times50$	$130\times90\times50$	$80\times60\times40$	$80\times60\times40$	$80\times60\times40$	$80\times60\times40$
No. of references used	1080	452	473	498	316	207	350
R (%)	3.35	2.44	3.08	2.26	2.00	3.61	1.85
wR (%)	4.05	3.02	4.39	2.65	2.37	2.38	2.11

and effective charges. Synchrotron radiation has important advantages for high-pressure single-crystal diffraction work: the intensive transmittance for the diamond anvils in the x-ray path, a high signal-to-noise ratio (S/N) for the diffraction intensities, and the detection of weak diffraction peaks. The tunability of SR energy also permits the use of an optimum wavelength. Because DACs have a small angular aperture that reduces the coverage of reciprocal space, the use of a short wavelength can mitigate this problem by allowing more reflections to satisfy the Bragg condition within the available angular range $(Q=2\sin\theta/\lambda)^2$.

In this experiment, we used a monochromatic beam with $\lambda=0.619\,07$ Å ($E=20.0137$ keV) produced by a Si (111) monochromater at BL-10A at the Photon Factory KEK, Tsukuba. A well-collimated incident beam of 100 μm was used and the evacuated guide pipe approached quite near to the DAC for reducing as much as possible the diffraction incident beam by the air. A four-circle diffractometer with a scintillation counter was used for the intensity measurements because a point detector can measure intensities more precisely and therefore lead to a more precise determination of the orientation matrix (UB matrix) than is possible with area detectors such as imaging plates (IPs) or charge-coupled device (CCD) detectors. The measurement of diffracted intensities was carried out using the step-counting method with the ϕ-rotation axis fixed. For the intensity integration, at least 100 steps were used for each reflection.

The cramp-type DAC with (100)-plane cut single-crystal diamond-backing plates[31] was used for the present diffraction study under pressures up to 30 GPa.[32] This type of backing plate has an advantage on the precise measurement of diffracted intensities. However, beryllium backing plates often used for single-crystal diffraction studies show the strong powder rings. A mixture of ethanol, methanol, and water (16:3:1) was used as a hydrostatic pressure-transmitting medium. The $KNbO_3$ crystal with dimensions of $40\times60\times30$ μm^3 was placed in a 200 μm hole in a spring-steel gasket (80 μm in thickness), which served as the sample chamber. A small ruby chip was also placed in the sample chamber to serve as a pressure marker through the use of the ruby fluorescence method.[33] Diffraction intensity measurements at pressures of 1.6, 4.8, and 5.7 GPa for the orthorhombic phase, 7.6 and 9.4 GPa for the tetragonal phase, and 10.9 GPa for the cubic phase were performed, and the intensities were converted to structure factors $F_{obs}(\boldsymbol{h})$ after correction for x-ray absorption and Lorentz-polarization effects. Intensity measurements at ambient pressure were also performed using a Mo $K\alpha$ laboratory source. Experimental conditions are summarized in Table I.

B. Structure refinement

Conventional structure refinements were first performed using the program RADY (Ref. 34) before the MEM calculation. Since the tetragonal and orthorhombic structures of $KNbO_3$ both have noncentric space groups, *P*4*mm* and *Cm*2*m* (*Amm*2), respectively, the crystallographic origin of the both structures was fixed at the K position (0 0 0).

Structure factors $F_{cal}(\boldsymbol{h})$ were calculated using fully ionized atomic scattering factors f_j, which were taken from the International Tables for Crystallography.[35] Anomalous dispersion parameters f' and f'' were taken into account in the atomic scattering factor: $f=f_0+f'+if''$. Least-squares refinement was conducted by minimization of Δ [$\Delta=\Sigma_{\vec{h}}w(\boldsymbol{h})\{|F_{obs}(\boldsymbol{h})|-|F_{cal}(\boldsymbol{h})|\}^2$]. Converged structure parameters for each pressure are presented in Table II.

The lattice parameters at each pressure were determined by least-squares calculation of the orientation (UB) matrix

TABLE II. Lattice parameters, atomic positional coordinates, and temperature factors.

Pressure (GPa)		0.0001	1.6	4.8	5.7	7.6	9.4	10.9
Lattice constants			Orthorhombic ($z=2$)			Tetragonal		Cubic
a (Å)		5.6992(6)	5.6806(17)	5.6330(10)	5.6247(32)	3.9653(5)	3.9491(11)	3.9430(7)
b (Å)		5.7202(6)	5.6840(16)	5.6373(10)	5.6346(13)			
c (Å)		3.9840(3)	3.9704(30)	3.9642(36)	3.9609(13)	3.9531(32)	3.9468(12)	
V (Å^3)		129.88(4)	128.20(10)	125.88(12)	125.53(10)	62.16(5)	61.55(4)	61.30(3)
K	x			0		0		0
	y			0		0		0
	z			0		0		0
	B_{iso}	0.682(9)	0.64(3)	0.62(3)	0.42(3)	0.44(2)	0.35(2)	0.68(1)
Nb	x			0		0.5	0.5	0.5
	y	0.4975(2)	0.4873(9)	0.4885(11)	0.4899(12)	0.5	0.5	0.5
	z	0.5	0.5	0.5	0.5	0.5151(10)	0.5189(9)	0.5
	B_{iso}	0.344(4)	0.36(1)	0.29(3)	0.26(2)	0.19(1)	0.19(1)	0.28(1)
O1	x			0		0.5	0.5	0
	y	0.5350(6)	0.5119(10)	0.4962(5)	0.4776(17)	0.5	0.5	0.5
	z			0		−0.0060(8)	−0.0042(10)	0.5
	B_{iso}	1.02(34)	1.05(10)	0.78(9)	0.59(10)	0.50(2)	0.43(1)	0.45(1)
O2	x	0.24799(5)	0.2380(11)	0.2510(13)	0.2542(19)	0.5	0.5	
	y	0.2803(4)	0.2580(10)	0.2583(14)	0.2633(18)	0	0	
	z	0.5	0.5	0.5	0.5	0.4956(9)	0.4971(8)	
	B_{iso}	1.92(2)	0.62(7)	0.55(2)	0.27(8)	0.35(9)	0.37(10)	

based on 25 reflections. The pressure dependencies of the lattice parameters of three high-pressure polymorphs are presented in Fig. 1. The orthorhombic structure transforms to the tetragonal phase at about 7.0 GPa and further to the cubic phase at about 10 GPa. These transition pressures determined by the single-crystal diffraction studies are slightly lower than those obtained by our powder-diffraction experiments. This is probably because the single crystal is more sensitive to external pressure due the presence of far fewer grain boundaries than in the powder.

The lattice parameters a and b of the orthorhombic $Cm2m$ phase noticeably decrease with pressure. Compression curves for lattice parameters a, b, and c of the orthorhombic phase continuously decrease and finally converged to the lattice parameter of the cubic phase above 10 GPa.

K-O and Nb-O bond distances, together with KO_{12} and NbO_6 polyhedral volumes, are presented in Table III. The K atom is 12-fold coordinated and Nb is located in the sixfold coordination site in all three polymorphs. In the cubic structure, the 12 K-O bonds and the 6 Nb-O bonds are equivalent, respectively, while both adopt several different lengths in the tetragonal and orthorhombic structures. The average bond distances ⟨Nb-O⟩ and ⟨K-O⟩ show almost the same compressibility behavior, resulting in an equivalent compressibility of the polyhedral volumes of KO_{12} and NbO_6 (Fig. 1). The tolerance factor, defined by $t=\langle \text{K-O}\rangle/\sqrt{2}\langle \text{Nb-O}\rangle$ continuously increases with pressure and reaches a value of $t=1.00$ for the cubic perovskite. (Note that the tolerance factor is normally defined as a ratio of ionic radii: $t=(r_K+r_O)/\sqrt{2}(r_{Nb}+r_O)$. These ionic radii as a function of pressure were difficult to determine, however.)

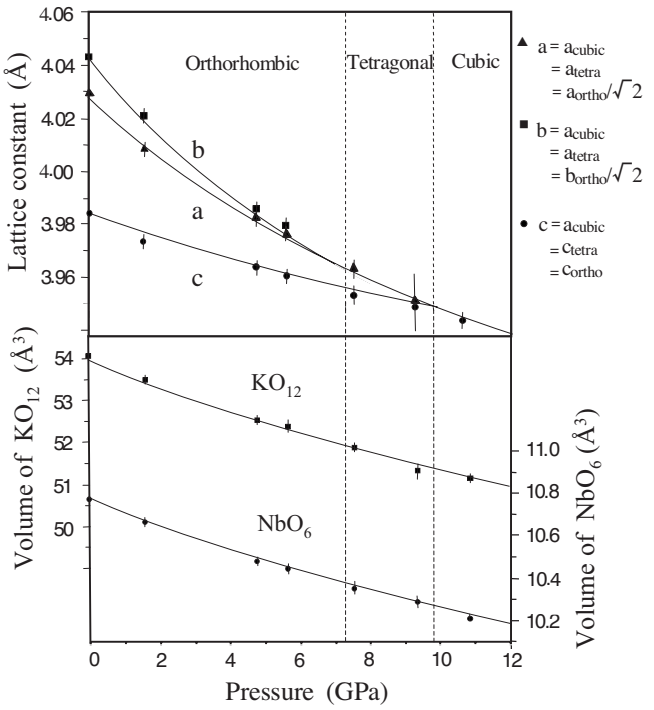

FIG. 1. Lattice parameters and cation-site volume change with pressure. Lattice parameters are determined by the orientation matrix based on the peak refinement of 25 reflections. The lattice parameters for the orthorhombic and tetragonal phases are normalized to that of the cubic phase. Pressure dependencies of the cation-site volumes of KO_{12} and VO_6 are presented in the lower part of the figure.

TABLE III. Interatomic distance, polyhedral volume, and tolerance factor.

Pressure (GPa)	0.0001	1.6	4.8	5.7		7.6	9.4		10.9
Bond length (Å)		Orthorhombic				Tetragonal			Cubic
K-O1	3.060(4)	2.910(6)	2.840(4)	2.943(4)	K-O1×4	2.804(4)	2.793(3)	K-O×12	2.788(4)
K-O1	2.660(4)	2.774(6)	2.7972(3)	2.695(4)					
K-O1×2	2.857(5)	2.841(4)	2.817(3)	2.815(4)					
K-O2×4	2.922(6)	2.814(9)	2.837(7)	2.858(9)	K-O2×4	2.812(2)	2.784(6)		
K-O2×4	2.759(7)	2.837(9)	2.784(9)	2.759(12)	K-O2×4	2.787(2)	2.800(6)		
⟨K-O⟩	2.846(7)	2.830(9)	2.812(8)	2.811(11)	⟨K-O⟩	2.801(2)	2.792(5)	⟨K-O⟩	2.788(4)
d/d_0	1.000	0.9944	0.9881	0.9877		0.9841	0.9810		0.9796
Nb-O1×2	2.004(7)	1.990(5)	1.983(4)	1.981(5)	Nb-O1	1.893(8)	1.882(1)	Nb-O×6	1.971(4)
Nb-O2×2	1.881(3)	1.878(9)	1.919(9)	1.917(9)	Nb-O1	2.060(9)	2.065(1)		
Nb-O2×2	2.164(9)	2.141(10)	2.069(18)	2.070(15)	Nb-O2×4	1.9841((5)	1.976(3)		
⟨Nb-O⟩	2.016(8)	2.003(9)	1.990(12)	1.989(13)	⟨Nb-O⟩	1.982(7)	1.975(3)	⟨Nb-O⟩	1.971(4)
d/d_0	1.000	0.9936	0.9871	0.9866		0.9831	0.9797		0.9776
Tolerance	0.9980	0.9990	0.9992	0.9993		0.9993	0.9996		1.0000
Polyhedral volume (Å^3)									
Vol. (NbO_6)	10.82(4)	10.68(2)	10.47(3)	10.46(5)		10.36(2)	10.30(2)		10.22(3)
$V/V_0(NbO_3)$	1.000	0.9871	0.9676	0.9667		0.9574	0.9519		0.9445
Vol. (KO_{12})	54.12(6)	53.42(4)	52.45(4)	52.31(5)		51.80(3)	51.25(4)		51.08(4)
$V/V_0(KO_{12})$	1.000	0.9870	0.9691	0.9665		0.9571	0.9469		0.9438

The equivalent temperature factors B_{eq} in Table II are presented in Fig. 2. The B_{eq} are related to the positional disorder and thermal vibration of the atoms. In the orthorhombic and tetragonal phases, they decrease with increasing pressure because the atomic-thermal vibrations are considerably restrained by the compression. However, the B_{eq} of all atoms of the cubic structure are enlarged due to the statistical distribution of atoms, as discussed below.

C. Electron density distribution by the maximum entropy method

The Fourier transform of the structure factors provides the electron-density distribution $\rho(xyz)$ in real space, whereas the difference Fourier synthesis ($|F_{obs}(\boldsymbol{h})|-|F_{cal}(\boldsymbol{h})|$) is applied in order to disclose the deformation electron-density distribution and the residual electron density $\Delta\rho(xyz)$, which express the nonspherical deformation in the electron density. Because the applied atomic scattering factor f_i indicates a spherical distribution with $\sin\theta/\lambda$, $\Delta\rho(xyz)$ is expressed by

$$\Delta\rho(xyz) = \frac{1}{V}\sum_h \sum_k \sum_l \{|F_{obs}(\boldsymbol{h})| - |F_{cal}(\boldsymbol{h})|\} \times \exp\{-2\pi i(hx+ky+lz)\}. \quad (1)$$

The radial distribution of the electron-density distribution describes the localization of electrons around atoms as a result of the deformation, which then has an effect on the dipole moment.

Fourier synthesis inevitably has a termination effect in the Fourier series. However, the difference Fourier synthesis can remove the termination effect in the observed electron-density distribution. Figure 3 shows the deformation electron density determined by the difference Fourier synthesis within the reciprocal space boundary set by $\sin\theta/\lambda < 1.22(\theta = 60°,\ \lambda = 0.7107$ Å) at ambient pressure. At high pressure, the small aperture angle of the DAC yields a limited set of diffraction data resulting in a small Q value. $F_{obs}(\boldsymbol{h})$ in this limited reciprocal space cannot provide a precise residual electron density or a picture of the bonding electron density from the structure refinement alone.

The electron-density distribution calculated by the MEM overcomes this problem and provides a much more reliable result. MEM statistically estimates the most reliable electron-density distribution from the finite structure factors. The termination effect found in the Fourier synthesis is therefore ignored. The "entropy" aspect of the MEM has its origins in information theory[36] and MEM was introduced to x-ray crystallography through several experimental and theoretical approaches[37–41] and was first applied to the problem of structure analysis.[42] The method has been extended and has become a more suitable and reliable process for structure analysis using single-crystal diffraction intensities.[43] A comparison of electron-density distributions calculated from the MEM and from multipole refinements has been reported.[44]

The MEM has often been applied for the analysis of electron-density distributions using powder-diffraction data.[45–48] The charge-density distribution in $KMnF_3$ under high pressure using powder diffraction has been investigated, for example.[48] Since the MEM is applied to structure factor data, the use of a large number of single-crystal diffraction intensities provides a much more precise result than those

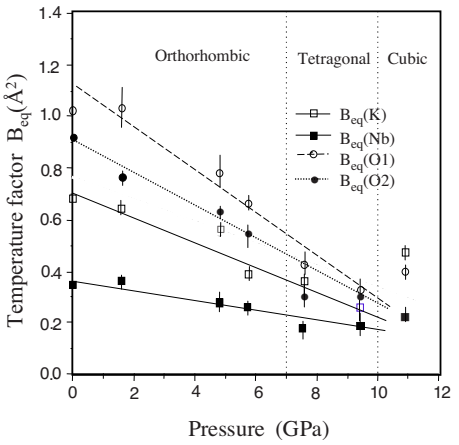

FIG. 2. (Color online) Pressure change in temperature factor B_{eq} indicating thermal vibration of atoms or atomic displacements.

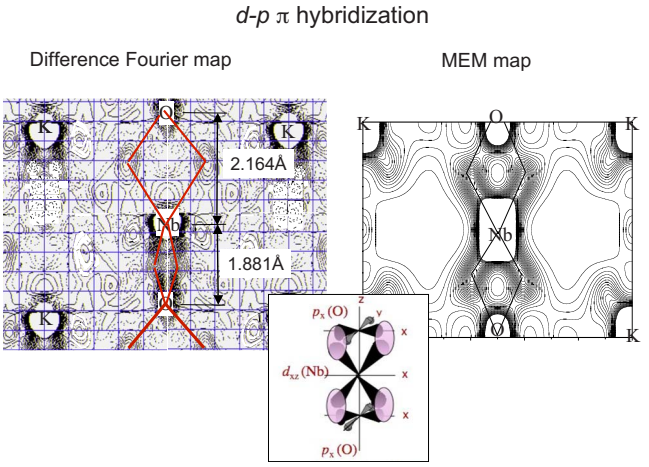

FIG. 3. (Color online) Difference Fourier map and MEM map of the orthorhombic phase ($Cm2m$) at ambient conditions. Projection onto (110) at $y=0.0$ using data set with $2\theta_{max}<120°$. The contour interval in the both maps is 0.2 $e/Å^3$. Positive and negative contours are expressed by solid and broken lines in the difference Fourier map, respectively. The residual electron-density distributions indicate d-p-π hybridization of the Nb-O bond.

from powder diffraction because the latter includes the ambiguity inherent in the deconvolution of overlapping peaks and a small number of observed data. On the other hand, single-crystal diffraction can directly measure $F_{obs}(\boldsymbol{h})$ individually for all reflections. Our previous test of the resolution of the MEM showed that a data set covering a larger reciprocal space showed a more precise electron distribution.[49] A much shorter wavelength may provide more precise information on bonding electron density even under high-pressure conditions.

The ideal entropy S is represented by

$$S = -\sum_{i}^{K} \rho'(\boldsymbol{r}_i) \ln \frac{\rho'(\boldsymbol{r}_i)}{\tau'(\boldsymbol{r}_i)}, \tag{2}$$

where $\rho'(\boldsymbol{r}_j)$ and $\tau'(\boldsymbol{r}_j)$ are the ideal electron density and the preliminary electron density, respectively. Specifically, $\rho'(\boldsymbol{r}_i)=\rho(\boldsymbol{r}_i)/\Sigma_i\rho(\boldsymbol{r}_i)$ and $\tau'(\boldsymbol{r}_i)=\tau(\boldsymbol{r}_i)/\Sigma_i\tau(\boldsymbol{r}_i)$, where $\tau'(\boldsymbol{r}_j)$ indicates the electron density one cycle before the iteration of the least-squares calculation of $\rho'(\boldsymbol{r}_j)$. $\rho(\boldsymbol{r}_j)$ is defined by

$$\rho(\boldsymbol{r}_i) = \tau(\boldsymbol{r}_i)\exp\left[\frac{\lambda F_{tot}}{N}\sum_{h}\frac{w(\boldsymbol{h})}{\sigma^2(\boldsymbol{h})}\{F_{MEM}(\boldsymbol{h}) - F_{obs}(\boldsymbol{h})\} \times \exp\{-2\pi i(\boldsymbol{h}\cdot\boldsymbol{r}_i)\}\right], \tag{3}$$

where N is the number of the observed structure factors $F_{obs}(\boldsymbol{h})$, λ is a Lagurange undetermined coefficient, and F_{tot} is the total number of electrons. The detailed derivation of the MEM using single-crystal diffraction intensities observed under high-pressure conditions was presented in our previous paper.[49]

The residual electron-density distribution can be derived from an aspherical electron-density distribution such as that corresponding to d electrons or the anharmonic-thermal vibration of atoms. However, the anharmonicity can be ignored in the present refinements because the Debye temperature Θ_D of $KNbO_3$ is much higher than room temperature.

The difference Fourier map confirms the participation of d-electron orbitals on Nb in site symmetry $m2m$, indicating the occupation of either $\boldsymbol{d}_{xz}$ or $\boldsymbol{d}_{yz}$ orbitals of the t_{2g} type at the octahedral site. The effective charge on the Nb ion is much smaller than the formal charge Nb^{5+} ($4d^0$) and so the Nb atom is not fully ionized. The residual electron density around Nb (Fig. 3) clearly indicates the presence of d-p-π bonding electrons due to the hybridization of the d orbitals on Nb and the p orbitals on oxygen.

Figure 3 also shows the MEM electron-density distribution between Nb and O in the (110) plane of the orthorhombic phase at ambient conditions using the same $F_{obs}(\boldsymbol{h})$ data as used for the difference Fourier synthesis. The diffraction angle using the DAC is indeed limited to 80° in 2θ but the MEM guarantees a sufficiently reliable electron density around the atoms. The same contour interval of 0.2 $e/Å^3$ was applied for comparison between two maps. It has been previously proved that contour lines with interval of 0.1 $e/Å$ give reliable information in MEM maps.[49]

MEM calculations reveal the deformation in the electron densities around K and Nb in the three different polymorphs. As seen from the projection onto (001) at 0.0001, 5.7, 9.4, and 10.9 GPa in Fig. 4, no obvious bonding electron density on the Nb-O bonds is found in the electron-density map. The tetragonal phase at 9.4 GPa has no polarization in any other direction than the [001] direction. A deformation in the electron density is observed in the orthorhombic phase, confirming the possible polarization in both [100] and [010] directions. Figure 5 shows the electron distribution maps projected onto (010) for the orthorhombic phase and onto (110) for the tetragonal and cubic phases. These maps suggest that the tetragonal phase has the largest polarization in the [001] direction among the three polymorphs.

The electron-density map of the tetragonal phase found at 9.4 GPa indicates the split Nb atoms (Fig. 4), where the Nb atom is statistically distributed at two positions along the c

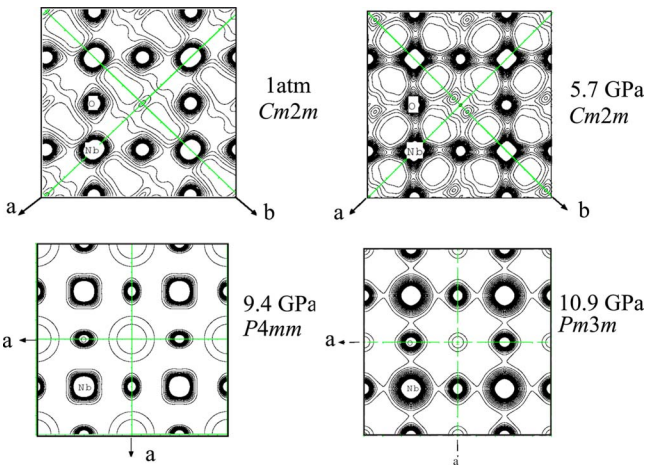

FIG. 4. (Color online) Deformation electron-density MEM maps projected onto (001) for the orthorhombic, tetragonal, and cubic polymorphs. The tetragonal phase at 9.4 GPa and cubic phase at 10.9 GPa have no deformation with the contour interval 0.2 $e/\text{Å}^3$ in the both maps, indicating no polarization in any direction perpendicular to [001].

axis because the thermal vibration of the atom obscures this feature at low temperature under ambient conditions. The electron distributions around the Nb and O atoms confirm the polarization in the [001] direction.

Generally the thermal vibration of atoms is restrained under compression, resulting in a smaller temperature factor B_{eq} with increasing pressure. The radial electron distribution on the O-Nb-O chain parallel to the c axis indicates that the localization of the electron density around the atoms is more

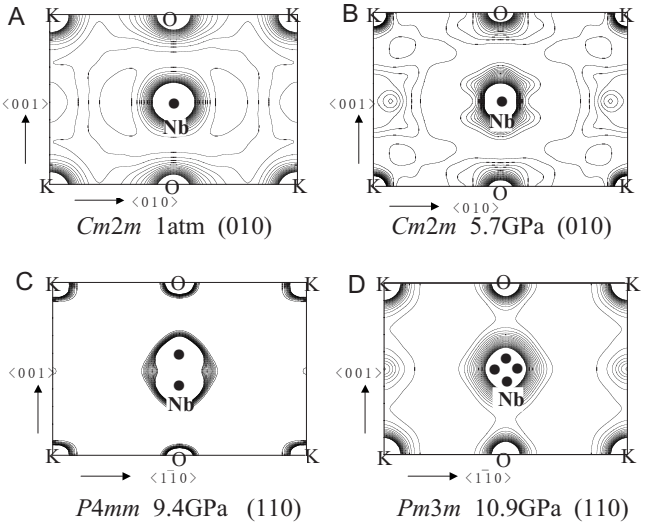

FIG. 5. MEM electron-density map at z=0.5. (a) Projection on the (010) plane at ambient conditions for the orthorhombic phase ($Cm2m$), (b) at 5.7 GPa for the orthorhombic phase, (c) projection on the (110) plane at 9.4 GPa for the tetragonal phase ($P4mm$), and (d) projection on the (110) plane at 10.9 GPa for the cubic phase ($Pm3m$). The contour interval is 0.2 $e/\text{Å}^3$. Solid circles indicate the estimated split Nb atomic positions. Nb atoms in the tetragonal and cubic structures are statistically distributed due to domain disorder.

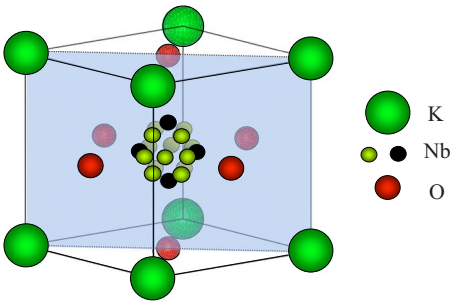

FIG. 6. (Color online) Schematic drawing of the statistical distribution of Nb atoms. Nb atoms are distributed at 6 positions in the direction of [100] as estimated from Fig. 4 and at 12 positions in the [110] direction as estimated from Fig. 5. A total of 18 split atoms are shifted from the inversion center. Black circles for Nb atoms are located on the (110) plane, which are indicated in Fig. 5.

enhanced in the orthorhombic and tetragonal structures with increasing pressure. The localization in the tetragonal phase at 9.4 GPa is most noticeable, which is consistent with the temperature factors of K, Nb, and O (Table II). However, the electron density around the Nb atom in the cubic phase at 10.9 GPa is much more diffused because all atoms are statistically distributed. The cubic phase is transformed from the tetragonal phase in which Nb atoms have two split positions. Consequently, the seemingly cubic phase is built up with the disordered structure of the noncubic phase and it becomes paraelectric. The individual domain structure does not have cubic symmetry.

After the observation of diffuse lines of $BaTiO_3$ by electron diffraction[50] and x-ray diffraction,[51] x-ray diffuse scattering experiments showed the presence of the [100] diffuse line in $KNbO_3$ and $BaTiO_3$.[52] An eight-site model of Nb atoms in $KNbO_3$ was proposed by Raman spectroscopy of $KNbO_3$ from 20 to 500 K at pressures up to 30 GPa, which indicated a ferroelectric transition based on the existence of the local disorder of Nb, whose atomic positions shift along the [111] direction.[21] The present electron distribution map of the cubic phase at high pressures in Figs. 4 and 5 indicates six positions in the direction of [100] and also twelve positions along [110] for Nb atoms rather than [111]. The present observation proposes the statistical distribution among 18 positions, as shown in Fig. 6. The dipole moments are canceled out in this model, indicating the paraelectricity of the macroscopic cubic phase of $KNbO_3$. With decreasing pressure the local disorder in the [001] direction becomes domi-

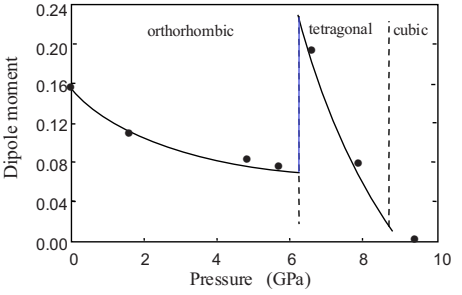

FIG. 7. (Color online) Change in the dipole moment with pressure in the direction of [001].

TABLE IV. Relative dipole moments.

Pressure	Nb			O1			O2×2					
(GPa)	Δx^+	Δy^+	Δz^+	Δx^-	Δy^-	Δz^-	Δx^-	Δy^-	$\Delta z^-\Sigma$	$\Delta y\Sigma$	Δz	Σr
0.0001	0.0	0.0	0.0025	0.0	0.0	0.035	0.0	−0.0020	0.0303	0.0020	0.1556	0.8901
1.6	0.0	0.0	0.0127	0.0	0.0	0.0119	0.0	−0.0120	0.0080	0.0120	0.0406	0.2308
4.8	0.0	0.0	0.0115	0.0	0.0	−0.0038	0.0	0.0010	0.0083	0.0010	0.0243	0.1369
5.7	0.0	0.0	0.0101	0.0	0.0	−0.0224	0.0	0.0042	0.0133	0.0042	0.0143	0.0806
7.6	0.0	0.0	0.0151	0.0	0.0	0.0060	0.0	0.0	0.0044	0.0	0.0239	0.0945
9.4	0.0	0.0	0.0189	0.0	0.0	0.0042	0.0	0.0	0.0029	0.0	0.0289	0.1140
10.9	0.0	0.0	0.5	0.0	0.0	0.0				0.0	0.0	

nant in the tetragonal phase and, with further decreasing pressure, the disorder in the direction of [110] becomes more obvious in the orthorhombic phase.

D. Dipole moment and effective charge

A spontaneous dipole moment $P_s=\Sigma q_i r_i$ is related to the distance r_i between point charges $+q$ and $-q$, where r can be given by the interatomic distances. Total positional displacement Δr of each atom is calculated by the divergence from the ideal interatomic distances (Table IV). The effective charge on Nb is increased due to the electron localization at higher pressure. This localization trend is the same feature as observed in SiO_2 stishovite with increasing pressure up to 30 GPa.[53] The electron localization corresponds to a large dipole moment associated with the Nb-O bond.

The effective charges of all atoms are determined by the monopole refinement (κ refinement),[54] in which the atomic-scattering factors are adopted as the variable parameters in the least-squares refinement. Atomic-scattering factors f_i are obtained from the wave function based on the Hartree-Fook approximation and these factors are presented in the International Tables for Crystallography.[35] The calculation using the isolated atom model gives an ideally spherical electron-density distribution. Effective charges of atoms are obtained from the following equation in the least-squares calculation using the shell model in which the core and valence electrons are separated as follows:

$$f(s/2) = f_{j,\mathrm{core}}(s/2) + P_{j,\mathrm{valence}} f_{j,M\ \mathrm{core}}(\kappa_j, s/2) + f_j' + if_j'', \tag{4}$$

where $s/2=\sin\theta/2\lambda$ and $P_{j,\mathrm{valence}}$ is the valence electron population on the atom j.

The atomic-scattering factor of the atomic core f_{core} is not variable, and the κ parameter is an indicator of the valence-electron distribution around a given atom. In the case of $\kappa=1$, the atomic-scattering factor is the radial distribution found in the International Tables for Crystallography,[35] where $\kappa>1$ represents more localized valence electron density. At ambient conditions, $P_{j,\mathrm{valence}}$ and the κ parameter are obtained from the structure refinement. $P_{\mathrm{Nb,valence}}$, $P_{\mathrm{K,valence}}$, κ_{Nb}, and κ_{K} of K and Nb are variable parameters in the present calculation: $P_{\mathrm{Nb,valence}}=+3.6(1)$, $P_{\mathrm{K,valence}}=+0.9(1)$, $\kappa_{\mathrm{Nb}}=0.84$, and $\kappa_{\mathrm{K}}=0.78$. $P_{\mathrm{O,valence}}$ is obtained from the constraint for the neutrality: $P_{\mathrm{O,valence}}=-(P_{\mathrm{Nb,alence}}+P_{\mathrm{K,valence}})/3=-1.5(1)$.

The effective charge on K, Nb, and O are represented by $P_{\mathrm{K,valence}}$, $P_{\mathrm{Nb,valence}}$, and $P_{\mathrm{O,valence}}$, respectively.

With the limited number of reflections observed due to the small diffraction angle of the DAC, it was not possible to resolve the effects of increasing pressure on these parameters. Given that the effective charge does not change in the present pressure range in spite of greater electron localization at higher pressure, the static dipole moment can be determined using the observed κ and Δr_i values in the direction of the c axis, as shown in Fig. 7. With increasing pressure, the dipole moment $\Sigma q_i \Delta r_i$ is lowered in the orthorhombic and tetragonal phases. After the transition from the orthorhombic to tetragonal phase, the moment is enhanced because the displacement along the c direction becomes much larger. This characteristic change is also consistent with our previous dielectric measurements.[26]

The MEM is an extremely efficient method for elucidating the electron-density distribution under high-pressure conditions. Because with the use of the MEM it is possible to ignore the termination effect of the Fourier series, precise diffraction intensities can provide a detailed electron-density distribution. An understanding of the ferroelectric properties of $KNbO_3$ can be obtained through an analysis of the static dipole moment as determined from the variation in effective charges as a function of pressure.

ACKNOWLEDGMENTS

We would like to express our gratitude to Stephen A. Gramsh, Carnegie Institution of Washington, for his internal review and editing our paper. The present investigation was performed under the auspice of KEK under Proposal No. 2002G199 for single-crystal structure analysis at BL-10A.

*t.yamanaka@kce.biglobe.ne.jp

[1] W. Cochran, Adv. Phys. **9**, 387 (1960).
[2] S. Aubry, J. Chem. Phys. **62**, 3217 (1975).
[3] G. Shirane, H. Danner, A. Pavlovic, and R. Pepinsky, Phys. Rev. **93**, 672 (1954).
[4] F. Jona and G. Shirane, *Ferroelectric Crystals* (Pergamon, New York, 1962).
[5] T. Ishidate, S. Abe, H. Takahashi, and N. Mori, Phys. Rev. Lett. **78**, 2397 (1997).
[6] I. A. Kornev, L. Bellaiche, P. Bouvier, P. E. Janolin, B. Dkhil, and J. Kreisel, Phys. Rev. Lett. **95**, 196804 (2005).
[7] A. Sani and M. Hanfland, J. Solid State Chem. **167**, 446 (2002).
[8] Z. Wu and R. E. Cohen, Phys. Rev. Lett. **95**, 037601 (2005).
[9] N. Jaouen, A. C. Dhaussy, J. P. Itie, A. Rogalev, S. Marinel, and Y. Joly, Phys. Rev. B **75**, 224115 (2007).
[10] P. E. Janolin, P. Bouvier, J. Kreisel, P. A. Thomas, I. A. Kornev, L. Bellaiche, W. Crichton, M. Hanfland, and B. Dkhil, Phys. Rev. Lett. **101**, 237601 (2008).
[11] M. Ahart, M. Somayazulu, R. E. Cohen, P. Ganesh, P. Dera, Ho-Kwang Mao, R. J. Hemley, Y. Ren, P. Liermann, and Z. Wu, Nature (London) **451**, 545 (2008).
[12] D. Gourdain, E. Moya, J. C. Chervin, B. Canny, and P. Pruzan, Phys. Rev. B **52**, 3108 (1995).
[13] J. C. Chervin, J. P. Itie, D. Gourdain, and Ph. Pruzan, Solid State Commun. **110**, 247 (1999).
[14] Y. Kobayashi, S. Endo, T. Ashida, L. C. Ming, and T. Kikegawa, Phys. Rev. B **61**, 5819 (2000).
[15] D. Gourdain, P. Pruzan, J. M. Besson, S. Klotz, J. C. Chervin, B. Canny, W. G. Marshall, J. S. Loveday, and M. Hanfland, Phys. Rev. B **65**, 054104 (2002).
[16] Ph. Pruzan, D. Gourdain, J. C. Chervin, B. Canny, B. Couzinet, and M. Hanfland, Solid State Commun. **123**, 21 (2002).
[17] Y. Nakamoto, K. Ohi, T. Okada, T. Nagai, and T. Yamanaka, Ferroelectrics **337**, 189 (2006).
[18] T. P. Dougherty, G. P. Wiederrecht, K. A. Nelson, M. H. Garrett, H. P. Jenssen, and C. Warde, Phys. Rev. B **50**, 8996 (1994).
[19] Z. X. Shen, Z. P. Hu, T. C. Chong, C. Y. Beh, S. H. Tang, and M. H. Kuok, Phys. Rev. B **52**, 3976 (1995).
[20] M. Shamim and T. Ishidate, Solid State Commun. **113**, 713 (2000).
[21] Ph. Pruzan, G. Gourdain, and J. C. Chervin, Phase Transitions **80**, 1103 (2007).
[22] A. I. Frenkel, F. M. Wang, S. Kelly, R. Ingalls, D. Haskel, E. A. Stern, and Y. Yacoby, Phys. Rev. B **56**, 10869 (1997).
[23] T. Mansingh, J. Phys. D **4**, 560 (1971).
[24] R. H. Kulkarni and S. G. Ingle, J. Phys. D **5**, 1474 (1972).
[25] D. Errandonea and E. Moya, Physica Status Solidi A **203**, R1 (1997).
[26] Y. Kobayashi, S. Endo, K. Deguchi, L. C. Ming, and G. Zou, Solid State Commun. **120**, 515 (2001).
[27] M. Posternak, R. Resta, and A. Baldereschi, Phys. Rev. B **50**, 8911 (1994).
[28] A. V. Postnikov and G. Borstel, Phys. Rev. B **50**, 16403 (1994).
[29] R. I. Eglitis, A. V. Postnikov, and G. Borstel, Phys. Rev. B **54**, 2421 (1996).
[30] I. A. Kornev and L. Bellaiche, Phase Transitions **80**, 385 (2007).
[31] T. Yamanaka, T. Fukuda, T. Hattori, and H. Sumiya, Rev. Sci. Instrum. **72**, 1458 (2001).
[32] T. Yamanaka and T. Fukuda, Phys. Chem. Miner. **29**, 633 (2002).
[33] H. K. Mao, J. Xu, and P. M. Bell, J. Geophys. Res. **91**, 4673 (1986).
[34] S. Sasaki and K. Tsukimura, J. Phys. Soc. Jpn. **56**, 4 (1987).
[35] T. D. Hahn, *International Tables for Crystallography* (Reidel, Boston, 1983).
[36] E. T. Jaynes, IEEE Trans. Syst. Sci. Cybern. **4**, 227 (1968).
[37] J. Navaza, Acta Crystallogr., Sect. A: Found. Crystallogr. **42**, 212 (1986).
[38] S. W. Wilkins, J. N. Varghese, and M. S. Lehmann, Acta Crystallogr., Sect. A: Found. Crystallogr. **39**, 47 (1983).
[39] A. K. Livesey and J. Skilling, Acta Crystallogr., Sect. A: Found. Crystallogr. **41**, 113 (1985).
[40] R. Narayan and R. Nityananda, Acta Crystallogr., Sect. A: Cryst. Phys., Diffr., Theor. Gen. Crystallogr. **38**, 122 (1982).
[41] G. Bricogne, Acta Crystallogr., Sect. A: Found. Crystallogr. **44**, 517 (1988).
[42] D. M. Collins, Nature (London) **298**, 49 (1982).
[43] K. Yamamoto, Y. Takahashi, K. Ohshima, F. P. Okamura, and K. Yukino, Acta Crystallogr., Sect. A: Found. Crystallogr. **52**, 606 (1996).
[44] M. Merli, A. Pavesi, and M. Ranzini, Phys. Chem. Miner. **29**, 455 (2002).
[45] M. Sakata, T. Uno, M. Takata, and R. Mori, Acta Crystallogr., Sect. B: Struct. Sci. **48**, 591 (1992).
[46] R. Y. de Vries, W. J. Briels, and D. Feil, Acta Crystallogr., Sect. A: Found. Crystallogr. **50**, 383 (1994).
[47] M. Sakata, T. Itsubo, E. Nishibori, Y. Moritomo, N. Kojima, Y. Ohishi, and M. Takata, J. Phys. Chem. Solids **65**, 1973 (2004).
[48] S. Aoyagi, S. Toda, E. Nishibori, Y. Kuroiwa, Y. Ohishi, M. Takata, and M. Sakata, Phys. Rev. B **78**, 224102 (2008).
[49] T. Yamanaka, Y. Komatsu, and H. Nomori, Phys. Chem. Miner. **34**, 307 (2007).
[50] G. Honjo, S. Kodera, and N. Kitamura, J. Phys. Soc. Jpn. **19**, 351 (1950).
[51] J. Harada and G. Honjo, J. Phys. Soc. Jpn. **22**, 45 (1953).
[52] S. Ravy, J. P. Itie, A. Polian, and M. Hanfland, Phys. Rev. Lett. **99**, 117601 (2007).
[53] T. Yamanaka, J. Synchrotron Radiat. **12**, 566 (2005).
[54] P. Coppens, T. N. Guru Row, P. Leung, E. D. Stevens, P. J. Becker, and Y. W. Yang, Acta Crystallogr., Sect. A: Cryst. Phys., Diffr., Theor. Gen. Crystallogr. **35**, 63 (1979).